Title
Soot morphology in a liquid-fueled, swirl-stabilized combustor

Journal
Combustion and Flame, 112(3)

ISSN
0010-2180

Authors
Fang, TC
Megaridis, CM
Sowa, WA
et al.

Publication Date
1998-02-01

DOI
10.1016/s0010-2180(97)00109-0

Soot Morphology in a Liquid-Fueled, Swirl-Stabilized Combustor

T. C. FANG
UCI Combustion Laboratory, University of California, Irvine, CA 92697-3550, USA

C. M. MEGARIDIS
Department of Mechanical Engineering, University of Illinois, Chicago, IL 60680, USA

and

W. A. SOWA AND G. S. SAMUELSEN*
UCI Combustion Laboratory, University of California, Irvine, CA 92697-3550, USA

The morphology of particulate soot formed in a liquid-fueled, complex-flow (i.e., turbulent, recirculating) combustor has been studied using thermophoretic sampling and transmission electron microscopy. Soot size information was obtained via computer-aided image analysis. Particle morphology was observed to be similar to that found in other combustion devices (i.e., nearly spherical primary particles fused into aggregate chains and clusters). Axial regions where soot nucleation, growth, agglomeration, and oxidation occur were identified. Primary particle size was observed to increase with combustor height, but the largest primary size reached is small compared to that observed in laminar diffusion flames. From calculated estimates of the specific soot surface growth and oxidation rates, the growth rate was found to be lower and the oxidation rate comparable to those for laminar diffusion flames. Aggregate sizes were also observed to increase with combustor axial location, and were found to be distributed in a lognormal manner during the particle inception and growth stages. Fractal dimensions for characteristic aggregate populations were determined to be around 1.8, and were independent of combustor axial location. The results suggest that cluster-to-cluster aggregation—and not surface growth—is the dominant soot aggregate growth mechanism in the complex-flow reactor. Comparisons with more traditional methods for soot size determination were made with moderate success.

NOMENCLATURE

A_a	projected area of an aggregate
A_p	mean cross-sectional area of primary particle
$d_{eq,a}$	aggregate area-equivalent diameter
$d_{eq,v}$	aggregate volume-equivalent diameter
d_p	primary particle diameter
D_f	fractal or Hausdorff dimension
f	specific surface growth rate
k_f	prefactor constant, Eq. 3
L_{mx}	projected maximum dimension of an aggregate
n	number of primary particles per aggregate
n_g	geometric mean number of primary particles per aggregate
N	number of particles measured in a sample
$P(n)$	equivalent lognormal distribution function
R	full radius of burner = 40 mm
R_g	radius of gyration of an aggregate
v	axial component of velocity
t_s	sampling time
V_a	total aggregate volume
x	burner height above nozzle plane

Greek Symbols

α	projected area exponent
ρ	soot material density
σ	standard deviation
σ_g	mean geometric standard deviation
ϕ	equivalence ratio
ω	specific oxidation rate

* Corresponding author.

0010-2180/98/$19.00
PII S0010-2180(97)00109-0

COMBUSTION AND FLAME 112:312–328 (1998)

Published by Elsevier Science Inc.

INTRODUCTION

Particulate soot is a product of incomplete combustion which can create a host of problems for both combustion hardware and the atmospheric environment. In combustion devices, soot increases radiative heat load to the combustor walls, and degrades materials in subsequent components through surface deposition. In the atmosphere, submicron soot particles pose a human health hazard, hamper visibility, and can modify meteorological conditions. A large body of literature exists on soot formation in classical flames [1, 2], and a few studies [3, 4] are available in configurations relevant to practical combustors.

While this group of studies has provided information on particle size and particle concentration, details of the morphology of soot and its spatial variation are limited. Intrusive sampling techniques have been recently revitalized due to their capability to provide particulate morphological data in classical flames and high-temperature aerosols. In this paper, we present the application of a thermophoretic sampling technique to a model gas turbine combustor. Our purpose is to provide morphological data that are valuable: 1) for the interpretation of optical measurements, and 2) to develop an understanding of the soot formation processes in a complex-flow combustor.

THERMOPHORETIC SOOT SAMPLING

The approach of this study is to: 1) directly sample soot in the flame using thermophoretic sampling, and 2) subsequently analyze the samples using transmission electron microscopy (TEM) and computer-assisted image analysis. Thermophoretic sampling is an intrusive sampling technique for soot extraction from high-temperature environments. Developed by Dobbins and Megaridis, its use has been applied to laminar diffusion flames [5–9], as well as unsteady buoyancy-dominated flames [10]. Thermophoretic sampling has also been used successfully to determine the morphological character of soot aggregates in the fuel-lean (overfire) region of turbulent gaseous flames [11]. The procedure collects soot particles suspended in hot gases onto a cold surface introduced in the aerosol field. The technique is especially attractive for soot morphology studies because its underlying mechanism of thermophoretic transport is independent of particle size and morphology for aerosols in the free-molecular and transition regimes [12–14].

This study represents a unique application of the thermophoretic sampling technique since the soot aerosol is transported in a highly turbulent flow in which a spray flame is stabilized by aerodynamically induced recirculation. Previous studies addressing soot size and morphology from practical combustors have been limited in number, and their soot size analysis is commonly preceded by complex extraction processes that manipulate and possibly alter the soot particles from their in-flame state. Soot sampling through flow tubes/probes, filtration, water dispersion, and/or aerodynamic impaction before EM analysis has been an accepted protocol [15–17]. Thermophoretic sampling has the advantage over these more traditional techniques in that flame-borne particles are directly deposited on a substrate surface that is subsequently analyzed by TEM without any further specimen preparation. Transport of submicron soot particles to the sampling surface is most affected by the soot volume fraction, the temperature gradient (which is transient according to the heat transfer and boundary layer flow characteristics), and the time duration that the grid is immersed inside the flame gases. In practice, the time of sampling is optimized by trial and error to cause a light collection (roughly 10% substrate area coverage), which helps to preclude particle stack-up and preserve the original identity of individual aggregates.

Results from the TEM analysis are two-dimensional images of the three-dimensional soot particles, from which projected areas and other related quantities can be found. Particle volumes are determined by assuming uniform primary particles, and by using an established empirical formula that relates the observed aggregate projected areas to the number of primary particles per aggregate. Large numbers of aggregates and primary particles (> 100) are measured in order to yield reliable

size distributions, fractal dimension (D_f), geometric mean diameter (D_g), and geometric standard deviation (σ_g).

EXPERIMENT

Combustor and Soot-Sampling System

The burner employed in this work was a vertically fired, 80 mm ID, swirl-stabilized combustion chamber, and is shown in Fig. 1. In past studies, the flow field of the combustor has been characterized using laser anemometry, and its sooting structure interrogated using light-scattering intensity ratioing and interferometry techniques [18, 3, 4]. The burner features a hollow-cone liquid-fuel spray, reaction stabilized by a swirl-induced recirculation zone, and an unswirled annular air shroud coaxial to the swirl air. The combustor has the turbulent, recirculating dome region characteristic of those found in gas turbine combustors. The annular air helps to provide closure to the recirculation zone and to restrain the reaction from contacting the combustor walls, thus providing a clean boundary condition that makes the reactor amenable to laser diagnostic measurements and modeling.

In this study, the fuel (petroleum-derived JP-4) was centrally injected via a Parker-Hannifin air-assist research atomizer that was maintained at an atomizer air-to-liquid mass ratio (ALR) of 2.5. The combustor was operated at atmospheric pressure, with an unreacted reference velocity of 7.5 m/s and an overall equivalence ratio of $\phi = 0.3$. The ratio of swirl to dilution air was 1.67. The nozzle air flow (which ranged from 2.4 to 4.85 scfm and constituted 3–6% of the total air flow) was not included in the reference velocity and stoichiometry calculations.

The combustor was lengthened in the present study to allow sampling access well downstream of the normal combustor exit ($x/R = 8$, radius $R = 40$ mm). The axial sampling locations accessible through ports on the combustor walls were $x/R = 3.0$, 5.0, 7.0, 10.0, and 15.1. These sampling heights, as well as the combustor configuration and soot-sampling system, are depicted in Fig. 1. The combustor was kept stationary, while the probe platform translated on a vertical guide.

Figure 2 is a still color photograph of the reactor at nozzle ALR = 2.5 (exposure of 250 ms). It shows the visibly sooty flame in the swirl-stabilized combustor at this operating

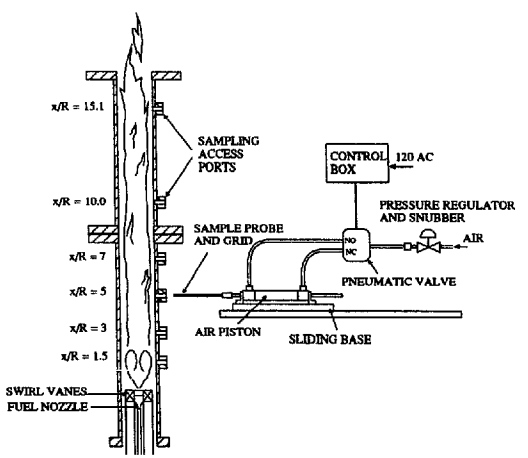

Fig. 1. Combustor and thermophoretic sampling system.

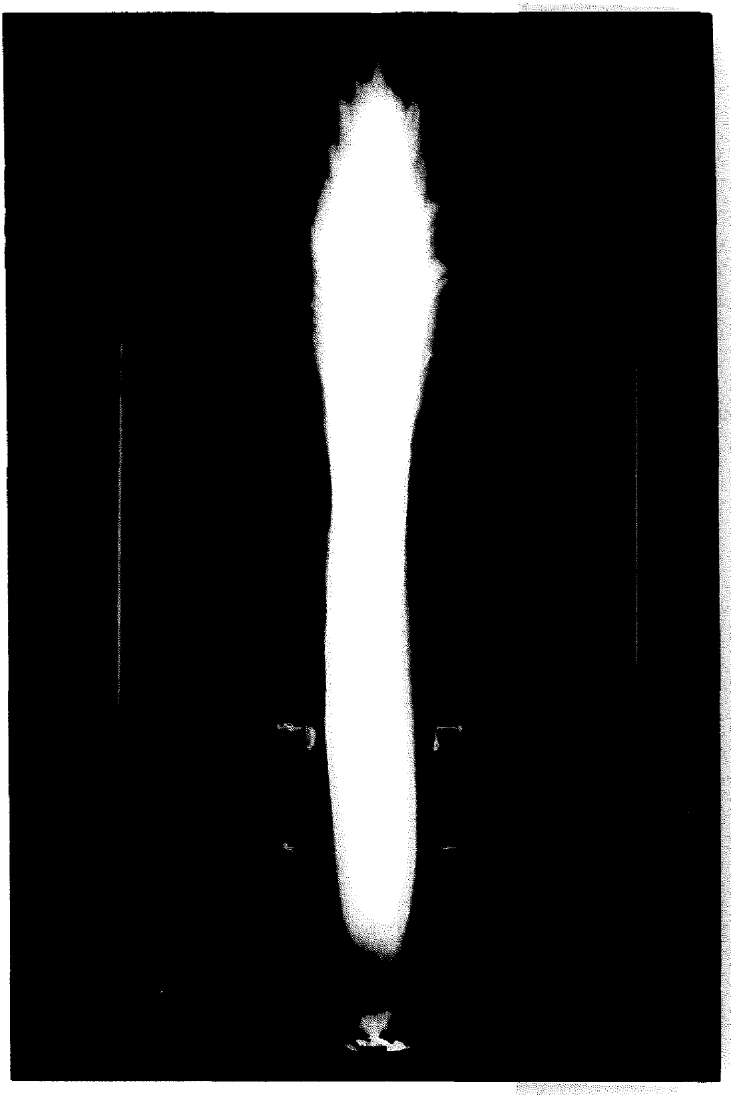

Fig. 2. Still photograph of the swirl-stabilized reaction at nozzle ALR = 2.5. A quartz pipe section is used.

condition. To obtain the photograph, the two-stage stainless steel combustor was removed and replaced with a quartz pipe, the length of which was about $10R$. Three flame regions can be seen in Fig. 2. The first is a blue region ($x/R = 0$–2) where the fuel vaporization and flame stabilization takes place. As shown in results that follow, soot inception is also occurring in this region. The following section from about $x/R = 2$–10 is a luminous core indicating the presence of radiating soot. This soot experiences significant burnout in the third region ($x/R > 10$) where the flame becomes unconfined and entrains ambient air.

Soot sampling was accomplished with a thermophoretic sampling system patterned after that used by Dobbins and Megaridis [5, 6]. The system includes a special sample collection surface, a rod probe, a pneumatic piston, a solenoid valve, and an electronic controller (see Fig. 1). The sampling surface is a standard TEM specimen grid coated with an elemental carbon substrate (200 Å nominal thickness). This provides the cold surface needed for thermophoretic deposition of soot. The specimen grid is mounted by a holding screw on a flat, vertical section at the tip of the cylindrical rod probe (1/8 in diameter). This rod probe is attached to a double-acting air piston which is powered by pressurized air from an electronically controlled solenoid valve. The sampling is accomplished by quickly inserting and retracting the rod probe with a specimen grid through the 1/4 in combustor ports. The time that the probe pauses inside the reactor (fully extended position) is the sampling time t_S, which can be varied using the electronic controller.

For the present study, a sampling time of $t_S = 60$ ms was adopted. The specimen grids were in transit to the reactor centerline, and thus exposed to the flame for approximately an extra 15 ms. The ratio of 4 to 1 in the sampling time at the center versus noncenterline positions was deemed sufficient to assume that the collected particles represented primarily the soot at the combustor centerline.

Different arrangements of the sample grid and probe that were tested included mounting the grid off the tip of the probe rod, as well as a horizontal orientation of the grid. Results with the vertical orientation of the grid were the best in the sense that grid survival and soot collection were the most consistent. Even though flow perturbation by the insertion and presence of the probe cannot be ruled out during soot sampling, consistent results obtained throughout our observations suggest that the intrusive nature of the sampling process does not alter the in-flame condition of the soot phase.

Soot Particle Size Analysis

Transmission electron microscopy (TEM) was used to examine the collected soot. TEM is especially suited for soot size and morphology observations with its high-resolution capability (down to 0.5 nm). Magnifications of 50,000 × and 115,000 × were used during soot observations with a Philips model CM20 TEM. Further photographic magnification resulted in the TEM micrograph prints used in soot size image analysis, with aggregate information extracted from micrographs of 133,000 × magnification and primary sizes from micrographs of 307,000 × magnification.

The quantitative analysis of the TEM electron micrographs was accomplished with the aid of a computer image analysis package called ImageSet (Dapple Systems, Inc., Sunnyvale, CA). The system was used to render micrographs of soot on a gray background into binary black/white images according to a threshold setting. Size and shape measurements produced by the program for an object of arbitrary shape included equivalent diameter based on projected area $d_{eq,a}$ and maximum linear dimension L_{mx}. Due to insufficient contrast between the soot flocculates and the micrograph background, manual tracing of the particle outlines was carried out before digitization and measurement took place.

As reported in similar studies, soot primarily consists of primary units that are almost spherical, and are bonded together to form cluster-like particles known as aggregates or agglomerates. The first step in soot size analysis was the measurement of primary particle size. This consisted of manually outlining unagglomerated particles or primary particles visible for each aggregate (usually around its perimeter), performing image analysis on the outline, and

then repeating the process for the aggregate itself. The respective results are equivalent-area diameters for primaries d_p and aggregates $d_{eq,a}$. It is important to note that d_p is an arithmetic mean value over the number of primaries traced for aggregates sampled from one flame location. On the other hand, $d_{eq,a}$ is a single value associated with each aggregate. Further analysis of the three-dimensional character of the particles was conducted by estimating the number of primary particles in each soot cluster, and then calculating its equivalent-volume sphere diameter.

The primaries per aggregate were estimated by using an empirical relation originally developed for carbon black morphology characterization and subsequently used for flame generated soot (see Refs. 9, 17):

$$n = (A_a/A_p)^{\alpha} = (d_{eq,a}/d_p)^{2\alpha} \quad (1)$$

where n is the number of primary particles in each aggregate, A_a is the observed projected area of the aggregate, A_p is the mean projected area of a primary particle, and α is a power factor accounting for the three-dimensionality of aggregates. A value of $\alpha = 1.09$ determined by Megaridis and Dobbins [9] was applied in this study, and reflects rather minor particle branching out of the plane of projection. This value is consistent with results of past computer simulations and TEM observations of soot and fractal carbon aggregates [9, 17]. The value of α adopted herein is almost identical to the value of $\alpha = 1.08$ determined by Koylu and Faeth [11] for their overfire soot aggregates. This approach was not directly validated for this study, but was deemed reasonable following visual inspection of the particle morphology.

The equivalent-volume diameter $d_{eq,v}$ for each aggregate was calculated from n by assuming spherical primary particles in point contact:

$$V_a = n(p/6)d_p^3$$

$$d_{eq,v} = (6V_a/p)^{1/3} = d_p(n)^{1/3} \quad (2)$$

where V_a is the volume of the aggregate. Uniform primary particles were assumed, with the average d_p of a population used in the calculation.

It is well established [9, 11] that soot aggregates exhibit mass fractal-like behavior, even though they do not strictly satisfy all conditions for fractal behavior. The number of primaries per aggregate n is thus related to the radius of gyration R_g of the aggregate and the fractal (or Hausdorff) dimension D_f through the power law expression

$$n = k_f(R_g/d_p)^{D_f} \quad (3)$$

where k_f is a prefactor. The radius of gyration R_g of an aggregate containing n primaries is defined in terms of the distance r_i of the center of each primary particle from the center of mass of the aggregate:

$$R_g^2 = \frac{1}{n}\sum_i r_i^2 \quad (4)$$

It is apparent that R_g data are difficult to obtain for soot aggregates since the exact three-dimensional structure of each aggregate is not known. However, it has been shown [19] that several alternate dimensions can be used in Eq. 3 instead of R_g in order to determine the fractal dimension. Since the maximum projected length L_{mx} of each aggregate was determined by the image analysis automatically, we used this quantity to determine D_f. In principle, the fractal dimension can be determined graphically for two or more aggregates by defining the slope of a $\ln n$ vs $\ln(L_{mx}/d_p)$ plot. Note that the prefactor in Eq. 3 is not required for D_f determination.

Our discussion so far has concentrated on individual aggregates as collections of primary units that comprise them. Each position within the combustor investigated herein is characterized by a set of parameters defining the population of aggregates transported through this location. A representative sample of these aggregates is captured by accurately positioning the sampling grid at a specific flame location, and is subsequently analyzed by image analysis. To this end, the expressions involving quantities defined previously for individual aggregates (n, d_p, $d_{eq,a}$, V_a, $d_{eq,v}$, R_g, D_f, etc.) are

also applicable for the mean quantities over the aggregate population characteristic of each location within the reactor. It is the primary goal of this work to examine the aggregate distribution parameters and their dependence on flame location.

Validation of thermophoretic soot sampling and the image analysis procedure was also conducted by evaluating the possible random and systematic errors. This included repeat measurements as well as comparison measurements using continuous sampling and size analysis using an electrical aerosol analyzer (EAA, TSI Model 3030) and scanning electron microscopy (SEM).

RESULTS AND DISCUSSION

TEM Micrographs

Figure 3 shows a series of TEM micrographs depicting soot sampled from five locations along the axis of symmetry of the reactor. These micrographs show soot aggregates that increase in size and display an increased degree of agglomeration as the sampling position moves downstream. There is moderate uniformity in the primary particle size at each axial location, although some variation does exist at all locations. An increase in primary particle sizes by heterogeneous surface growth is particularly visible between $x/R = 5.0$ and 10.0. Between $x/R = 10.0$ and 15.1, the qualitative observation can be made that agglomeration continues while the size of the primary particles diminishes somewhat. The above observations are quantified through computer analysis results presented in the following sections.

The polydisperse solitary particles present at the lower x/Rs (especially $x/R = 3$ and 5) have also been observed on the fuel-rich side of buoyancy dominated, gaseous flames [10], and conform to the description of the particles observed in low-pressure premixed flames [20]. These particles, also known as *microparticles* [10], vary in size up to 15 nm, are typically singlets or doublets, and appear rather transparent to the electron beam, possibly a result of their higher hydrogen content. As reported in Ref. 10, these particles possibly consist of mixtures of polyaromatic hydrocarbon fragments, and are likely precursors to carbonaceous soot. As dehydrogenation proceeds for soot transported along the axis of the reactor, the aging soot aggregates appear to be less transparent to the electron beam (compare micrographs at $x/R = 3.0$ and 15.1).

The relative absence of unagglomerated primary particles in the downstream regions of the combustor suggests that the inception of soot is restricted to the lower or dome regions of the reactor. The number of soot aggregates on each micrograph declines with combustor height,[1] suggesting a lower soot number density, consistent with expectations of an aerosol system undergoing agglomeration without continued nucleation.

Primary Particle Size

Figure 4 shows the progression of primary particle size distribution with burner height along the axis of the flame. Each of the histograms represents d_p measured from one micrograph. Other data sets from this study agree well with the information presented here (see Section 4.5.2 on data repeatability). The mean d_p, standard deviation σ, and number of primaries N measured for each distribution are indicated. This histogram series shows no size increase from $x/R = 3.0$ to 5.0, a significant increase from $x/R = 5.0$ to 10.0 (from 9.6 to 13.2 nm) due to surface growth reactions, and the onset of size decrease due to oxidation between $x/R = 10.0$ and 15.1. In addition, the ratio of σ/d_p is confined in a narrow region (0.15–0.24), which is in agreement with the values reported by Megaridis [6], as well as by Koylu and Faeth [11]. However, our values of σ/d_p increase with burner height, opposite to results from the laminar diffusion and diffusion flames of Refs. 6 and 11. The observed trend for primary size is presented in Fig. 5, which is a plot of the mean d_p values versus

[1] Measurements by the EAA indicated that the soot concentration is $\sim 10^9$ particles/cm^3 in this region and decreases slightly with height. It is interesting to note that a concentration of $\sim 10^8$ particles/cm^3 was found for a flame with ALR = 3.0, whose blue appearance suggests lower sooting characteristics.

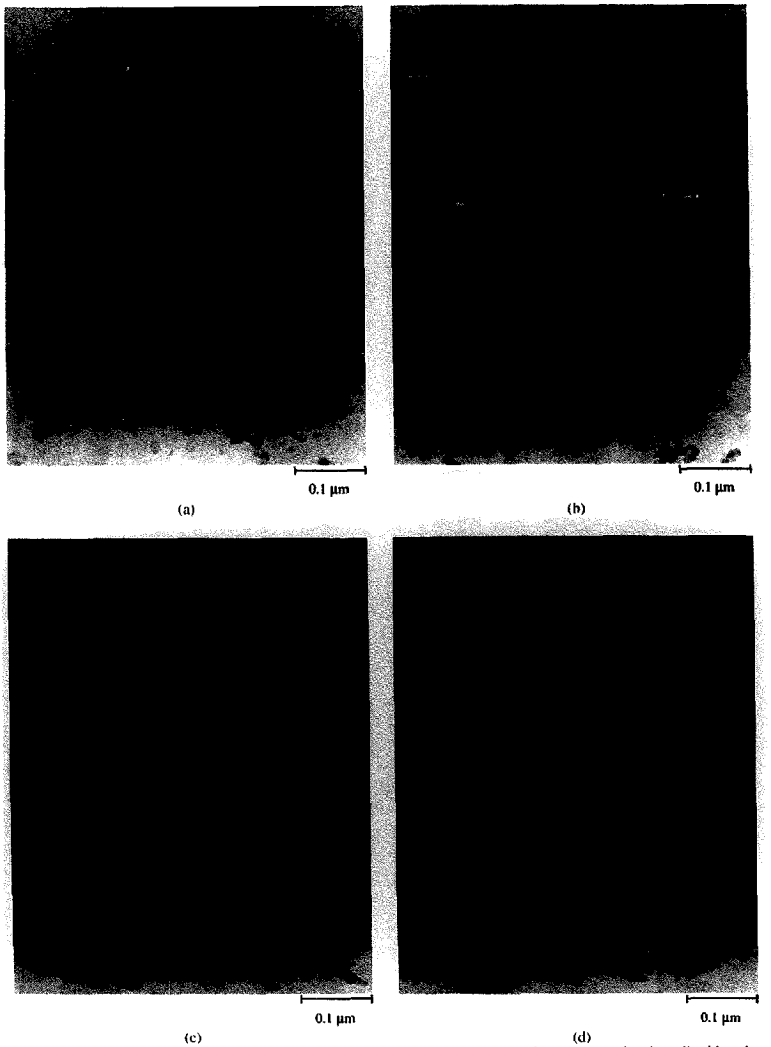

Fig. 3. TEM micrographs of soot sampled from the model combustor operating at a nozzle air-to-liquid ratio (ALR) of 2.5 at five locations along the axis. (a) $x/R = 3.0$, (b) $x/R = 5.0$, (c) $x/R = 7.0$, (d) $x/R = 10.0$, (e) $x/R = 15.1$.

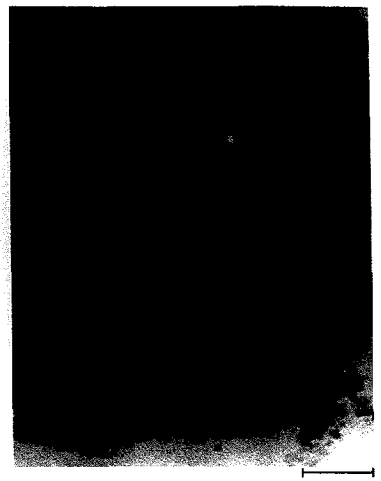

(e)

Fig. 3. *Continued*

axial distance. Thus, the determination of d_p for this combustor has revealed the regions where soot nucleation prevails, and where surface growth and oxidation occur. The error bars in Fig. 5 represent electron microscope magnification uncertainty of 3%.

The magnitude of the mean values of d_p observed along the axis of symmetry of the spray flame investigated herein covers the lower range of primary sizes observed in a wide variety of combustion systems. The entire range as reported in the literature is remarkably "narrowly confined" between 10–50 nm [9]. For example, the values of d_p reported by Megaridis and Dobbins [5, 9] for laminar, coannular diffusion flames are in the range of 12–35 nm. Koylu and Faeth [11] reported mean values of d_p between 30 and 50 nm in their overfire soot measurements. Wey et al. [21] found primary spherule sizes of 14–20 nm in a Gaydon and Wolfhard propane diffusion flame. Samson et al. [17] measured soot primary sizes to be 20–30 nm in a coannular diffusion acetylene flame. Vuk et al. [22] found primary particle diameters to be within 20–30 nm for diesel engine particulates. All of these determinations were conducted through TEM observations. Other comparable results are available in the compilation of previously reported values by Megaridis and Dobbins [9]. The narrow range of primary sizes, including those found in the current study, suggest similar soot formation mechanisms in widely different combustion systems.

The growth in primary particle sizes observed along the axis of the combustor considered herein is small compared to that observed in laminar hydrocarbon diffusion flames [5]. This is likely due to the low residence times in this complex-flow reactor. Residence times for this swirling flow are estimated from previous flow velocity measurements [23] to be 17 and 24 ms at $x/R = 10$ and 15, respectively. These times are only about a third of the residence times (about 70 ms) reached by soot particles in the laminar flame studied by Megaridis [6].

Other factors that can account for the difference observed in soot primary sizes include a difference in the soot growth rate of the two flames. An estimation of the growth and oxidation rates is made below.

Surface Growth and Oxidation Rates

From Ref. 8, we find that given the variation of d_p with axial distance and the axial particle velocity, one can calculate the specific surface growth rate f and specific oxidation rate ω for soot along the combustor centerline by the formula

$$f = -\omega = \frac{\rho v}{2} \frac{d(d_p)}{dx} \tag{5}$$

where ρ is the soot material density and v is the axial particle velocity. This formula for the growth and oxidation rates of primary particles also gives the rates of growth and oxidation for aggregates, when one assumes monodispersed primary particles, and that the presence of multiple particles within an aggregate does not affect their individual variations (point contact assumption).

A soot material density value of 1.86 g/cm^3 was used, and an estimate for the axial particle velocity was taken from laser anemometry measurements of the mean, reacting flow ve-

locity. With the same information that allowed for estimates of the flow residence times [23], we averaged the axial flow velocities measured at the plane of $x/R = 5$, and assumed that to be equal to the particle velocity (a justifiable assumption given the submicron size of the soot). The velocity was thus determined to be $v = 25$ m/s which, along with d_p data presented in Fig. 5, produced the values of f and ω given in Table 1. Acceleration of the flow downstream of $x/R = 5$ is likely, but velocity data were not available. Therefore, we take the value of f to be characteristic of the centerline region from $x/R = 5$–10, while the calculated ω can only be viewed as a first-order approximation for the region of $x/R = 10$–15.

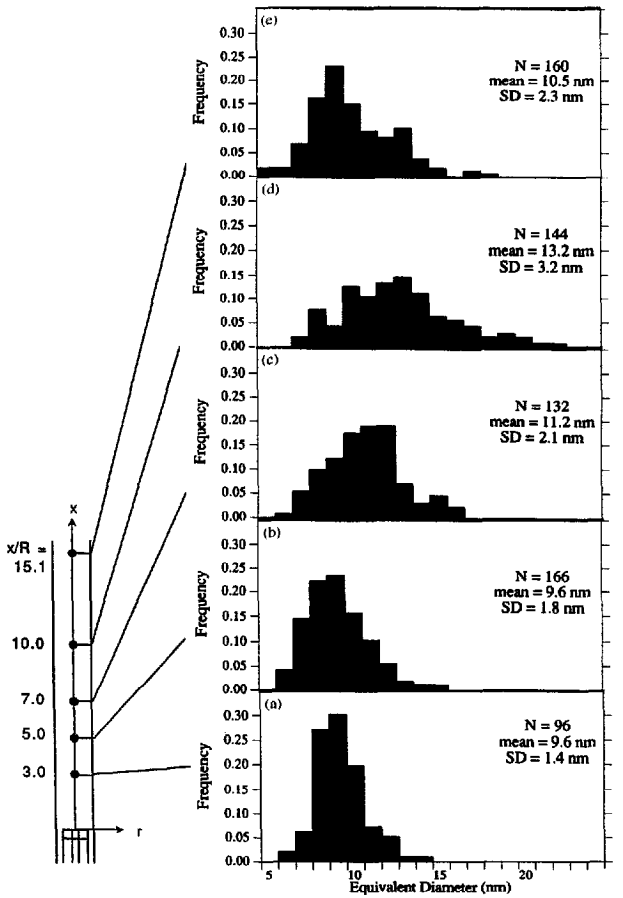

Fig. 4. Particle size distributions of soot primary particles measured from TEM micrographs. (a) $x/R = 3.0$, (b) $x/R = 5.0$, (c) $x/R = 7.0$, (d) $x/R = 10.0$, (e) $x/R = 15.1$.

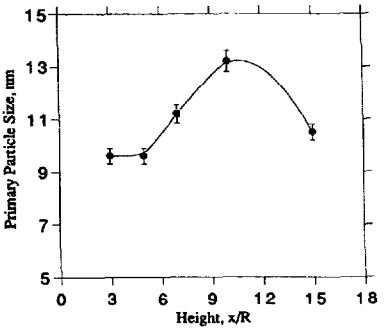

Fig. 5. Plot of the mean primary particle size vs burner height. Error bars represent 3% uncertainty in TEM size measurements.

Comparison of these results with those found in laminar diffusion flames reveals that the growth rate is somewhat lower, while the oxidation rate is comparable. The growth rate of 4.2×10^{-5} g/cm^2 s is roughly a factor of 2 below that reported by Megaridis and Dobbins [8], while being comparable to growth rates reported by Harris and Weiner [24] for a premixed flat flame (see Ref. 8 for comparison). The oxidation rate determined in the current study is comparable to the values of $3-5 \times 10^{-5}$ g/cm^2 s reported in [8] for a soot-releasing, smoking, laminar diffusion flame. However, this rate is substantially lower than those reported in [8] for a nonsmoking diffusion flame.

The lower surface growth rate in this complex-flow combustor compared to laminar diffusion flames likely contributed to the smaller primary particles sizes observed. Factors that can affect the surface growth rate include the amount of soot (i.e., particle surface area) formed in the inception stage [25], the temperature history of the particles, and the concentrations of the precursor and oxidizer species. Because intense mixing of fuel and air occurs in the dome region ($x/R = 0-3$), soot growth may also be slower due to competition with oxidation reactions throughout the pyrolysis, inception, and surface growth stages.

TABLE 1

Specific Soot Growth and Oxidation Rates for Soot Sampled from the Combustor Centerline

x/R	Specific Rates, g/cm^2 s
5–10	$f = 4.2 \times 10^{-5}$
10–15	$\omega = 3.1 \times \times 10^{-5}$

Aggregate Statistics

Figure 6 presents histograms of the equivalent-area diameter $d_{eq,a}$ distributions of the soot transported along the combustor axis with respect to combustor axial height. Bin widths of 5 nm were used in the histograms, and the sum of all the areas of the bars has been normalized to unity. The number of aggregates N used for the determination of each histogram is also listed in that figure. The histogram series shows a shift toward larger sizes with axial distances between $x/R = 3$ and $x/R = 10$. This is a result of soot particle growth by both agglomeration and surface growth in the swirl-stabilized combustor. Between $x/R = 10$ and 15.1, agglomeration continues, but the oxidation mentioned earlier is also taking place, thus resulting in a wider distribution including large aggregates as well as a pronounced peak at smaller aggregate sizes (10–15 nm). The small sample size ($N < 100$) at the two higher axial locations means that the distributions measured at these heights are not as statistically sound as those at lower regions. In particular, data for $x/R = 15.1$ reported here and elsewhere in this paper are used to reveal trends, but their reliability is limited.

Equation 1 was employed to calculate the number of primary particles per soot aggregate measured. This procedure was repeated at each axial location. The resulting distributions of n are plotted in Fig. 7. Mean values of n were observed to increase by nearly threefold from $x/R = 3$ to $x/R = 10$, and are tabulated in Table 2 as n_{avg}. These results again demonstrate the trends of aggregate growth with axial distance and the development of broader distributions at the upper burner positions.

Soot aggregate distribution information is important for both the interpretation of optical measurements and the modeling of soot for-

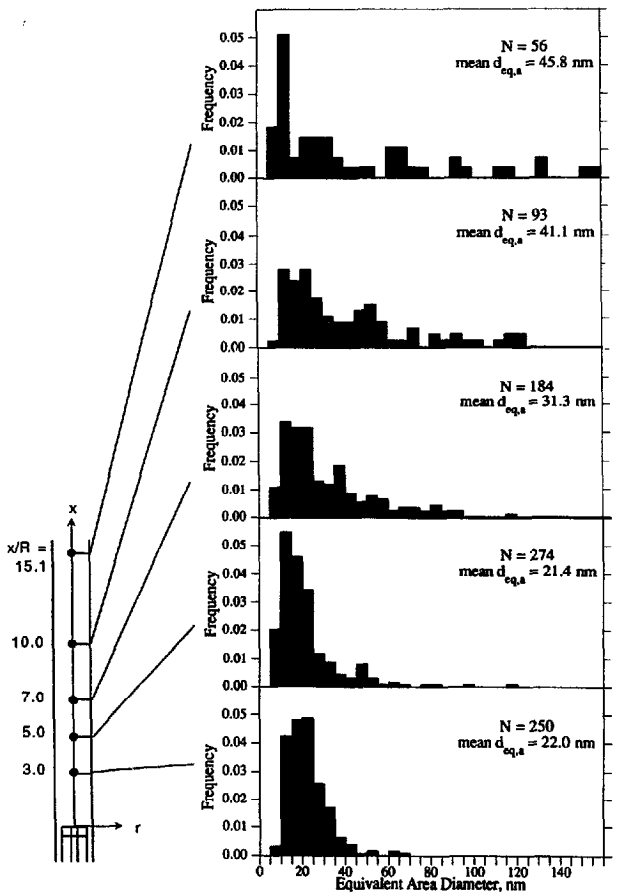

Fig. 6. Variation of soot aggregate equivalent-area diameter distributions $d_{eq,a}$ with burner height. Equivalent area diameters were measured from TEM micrographs.

mation. Past studies have used assumptions of self-preserving [24] and lognormal [26] distributions in their modeling or analysis. Lognormal soot size distributions have been suggested by past experimental evidence as well [20, 27, 28]. Equation 1 was employed to calculate the number of primary particles per soot aggregate measured. This procedure was repeated at each axial location. The resulting distributions are plotted in Fig. 7 (solid black bars). These again demonstrate the trends of aggregate growth with axial distance and the development of broader distributions at the far downstream upper positions. Figure 7 also makes a qualitative comparison of the experimental data with the equivalent lognormal distribution and the

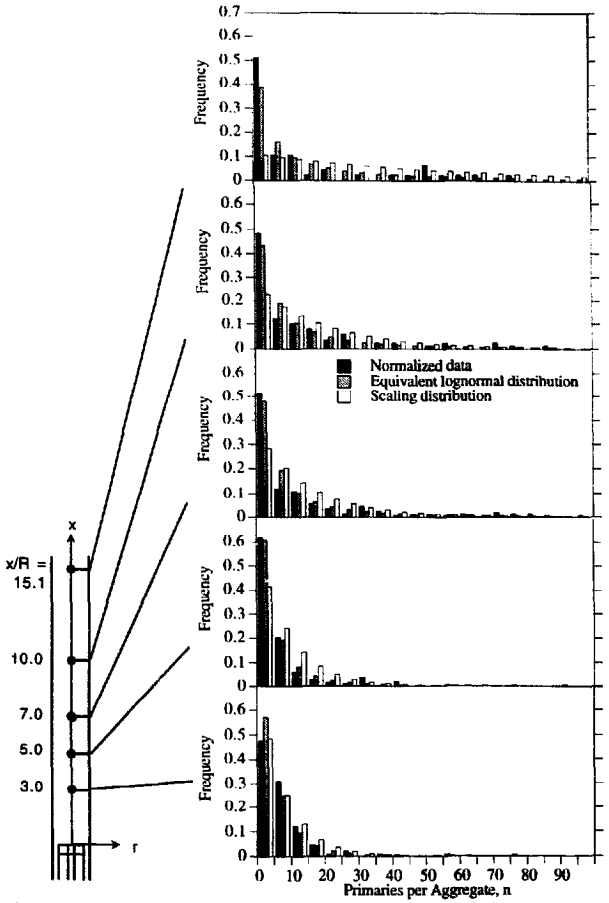

Fig. 7. Comparison of number of primaries per soot aggregate distribution with the equivalent lognormal distribution and the scaling distribution from Sorensen et al. [31].

scaling distribution that is described by Sorenson et al. [31]. The scaling distribution used is the simplest form which is applicable to coalescing particles in the free molecular regime ($e^{-n/n_{avg}}$). The equivalent lognormal comparison is accomplished by first determining the geometric mean number of primary particles per aggregate n_g and standard deviation σ_g of the distributions of n corresponding to the five heights considered herein.

The geometric mean number of primaries per aggregate n_g of the distribution of aggregates at each location was calculated by

$$\ln n_g = \frac{\Sigma_i \ln n_i}{N} \tag{6}$$

where the summation extends over all aggregates according to the procedure described earlier. N is the total number of aggregates measured at each combustor height.

The mean standard deviation σ_g of the aggregate distribution at the same location was determined from

$$\sigma_g^2 = \frac{1}{9N} \sum_i \left(\ln \frac{n_i}{n_g} \right)^2. \tag{7}$$

The equivalent lognormal distribution of n corresponding to each pair of n_g, σ_g is then given by

$$P(n) = \frac{\exp\left\{ -\left[\frac{(\ln(n/n_g)}{3\sigma_g 2^{1/2}} \right]^2 \right\}}{3n\sigma_g (2\pi)^{1/2}} \tag{8}$$

where n is the mean value within each bin.

In Fig. 7, there is modest agreement between the experimentally obtained soot aggregate distribution and the corresponding equivalent lognormal distributions. This agreement is better than that with the scaling distribution, particularly early in the reaction. Note that the small ($N < 100$) aggregate samples at higher axial locations ($x/R = 10$ and 15.1) are partially responsible for the low smoothness of the experimentally obtained distributions. For this system and operating condition, the lognormal distribution is a fair estimate of the soot aggregate size distribution in the nucleation and surface growth zones of the model combustor. The lognormal curve becomes less accurate for representing the size distribution at the upper regions of the combustor where agglomeration occurs simultaneously with oxidation.

The geometric mean value of n_g and standard deviation σ_g of the aggregate distributions are also key parameters used for comparison between soot populations from various combustion systems. The values of n_g and σ_g calculated for the conditions investigated herein are tabulated in Table 2 as a function of height x/R above the nozzle. In comparison, σ_g values determined for laminar, diffusion flames are in the range of 0.3 and 0.4 [9]. The corresponding values for overfire soot also fall within this range [11]. Mean values of d_p, n, and $d_{eq,a}$ from $x/R = 3$–15 are also tabulated in Table 2.

Figure 8 depicts the determination of fractal dimension D_f by a log–log plot of n vs L_{mx}/d_p (maximum linear dimension of aggregate over mean primary size). The straight line fitted through the aggregate data represents the best fit. The slope of this line (see Eq. 3) defines the fractal dimension at each location (also tabulated in Table 2). There is no trend observed with x/R in the D_f results, as expected. As with numerous previous studies (see summary of earlier measurements in Ref. 9), which found D_f for soot or carbon black aggregates, our values of about 1.8 suggest the dominance of diffusion-limited, cluster-to-cluster agglomeration. This means that diffusional factors outweigh factors of free-molecular collision or chemical reaction in the agglomeration processes, and that aggregation is dominated by collisions between aggregates mostly, instead of collisions between primary particles with aggregates.

TABLE 2

Soot Aggregate Parameters as a Function of Nondimensional Flame Height; Values at $x/R = 15.1$ Are Not as Reliable as Those at Lower Heights Due to Limited Sample Size

x/R	$d_{p,avg}$ (nm)	n_{avg}	$d_{eq,a,avg}$ (nm)	n_g	σ_g	D_f
3	9.6	7.55	22.0	5.14	0.28	1.75
5	9.6	9.37	21.4	4.07	0.38	1.85
7	11.2	15.2	31.3	5.97	0.45	1.85
10	13.2	19.8	41.1	7.15	0.48	1.81
15.1	10.5	53.9	45.8	9.63	0.66	1.84

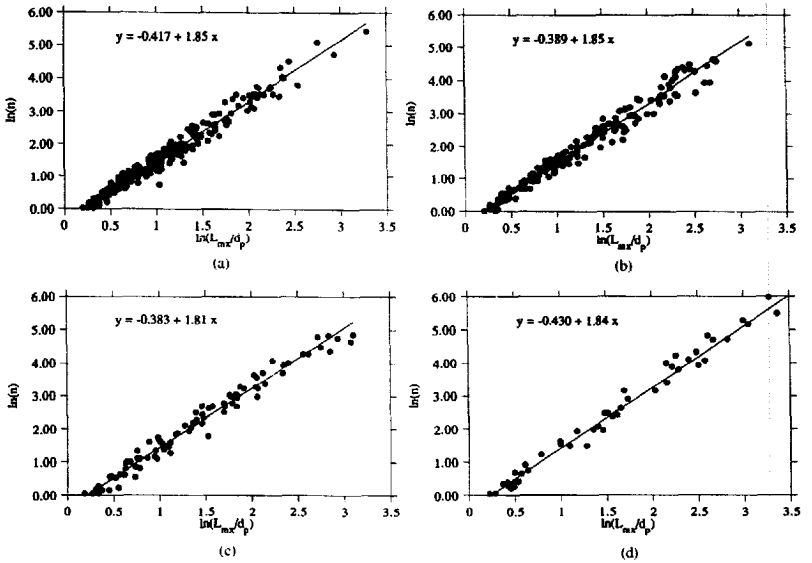

Fig. 8. Plots of $\ln n$ vs $\ln(l_{max}/d_p)$ at four different heights along the axis of the flame. The fractal dimension D_f for each height is defined by the slope of the corresponding straight line fits. a) $x/R = 5.0$, b) $x/R = 7.0$, c) $x/R = 10.0$, d) $x/R = 15.1$.

Error Analysis

Both random and systematic errors were considered as sources of possible inaccuracies or biases in the sampling and data analysis processes. Errors due to random factors in thermophoretic soot sampling and the image analysis procedure were estimated through repeat tests, or replication. Efforts to identify systematic errors consisted of independent size measurements using EAA and SEM analysis (Section 4.6).

Errors in individual values of d_p and $d_{eq,a}$ are related to the resolution accuracy of the technique, and were evaluated by identifying error sources in the image analysis steps and considering their propagation (Section 4.5.1). The random errors of statistical quantities such as mean d_p and $d_{eq,a}$ were estimated using a statistical treatment as follows. The error associated with the mean d_p was computed from the standard deviation σ of the size distributions according to the following equation [29]:

$$\delta d_p = \sigma / N^{1/2} \tag{9}$$

where N is the number of samples included in the mean and standard deviation calculation. Results of δd_p using the data presented in Fig. 4 range from 0.1 to 0.3 nm. Similarly, uncertainty in the means of $d_{eq,a}$ range from 0.6 to 6.0, the larger errors being associated with higher axial regions that are characterized by wider distributions and smaller values of N.

Errors in Image Analysis

Errors introduced during the computer image analysis tended to be random in nature, with the possible exception of the TEM magnification. As seen in Fig. 5, an estimate of this error

on any given day is 3%. This uncertainty is variable, or random, from day to day, but is a source of systematic error for a data set acquired during any single day.

A systematic bias in the tracing process (i.e., over- or undertracing of the particle outline) was carefully avoided. Furthermore, evaluation of possible operator bias in the particle tracing process was conducted by having two operators trace approximately 70 aggregates from the same micrograph. The discrepancy in the mean equivalent area diameter resulting from the two data sets was only about 3% in the evaluation.

Two possible sources of error arising from the computer image analysis are inaccuracies due to the coarseness of the pixel grid, and manual selection of a threshold grayness level for binary digitization. Multiple measurements of 17 particles with two pixel size units gave discrepancies as high as 7%, with the finer pixel sizes (more pixels per unit length) being more accurate. For the data presented in this paper, pixel sizes of about 1600 pixels/mm were used for d_p determination, and about 700 pixels/mm were used for aggregate size determination (due to different magnification). For the issue of gray threshold selection, this has a bearing on particle size since it affects the definition of the perimeters. Repeat tests of manually using different yet reasonable threshold levels for one micrograph gave results that agreed within 3%.

Errors from both limited pixels and subjective threshold selection were evaluated using a computer-derived set of 110 round dots. The mean size of the dots obtained under similar pixel size and threshold conditions as was used for the soot analysis deviated about 1% from the exact value.

Repeatability of Results

The repeatability of the results was checked by taking aggregate size data from eight micrographs originating from three different grids sampled at $x/R = 10$, and performing the *equality of means* test on this data set [30]. The test results suggested that the $d_{eq,a}$ data sets resemble one another closely enough to be considered as belonging to the same population. The consistency between micrographs implies that data from one micrograph are likely representative of the in-flame sampled soot population.

SEM and EAA Comparison

Attempts to pinpoint possible systematic errors in the thermophoretic sampling and TEM analysis by using scanning electron microscope (SEM) observations and an electrical aerosol analyzer (EAA) had limited success. We note that the SEM and EAA measurements involved a continuous extraction of the particles from the flame environment using a stainless steel probe and subsequently cooled with dilution air. Quenching at the probe tip was not accomplished. SEM data gave similar qualitative data on particle morphology, but gave results biased toward larger sizes. This was primarily due to a conductive gold/palladium coating (nominally 10 nm thick) required by SEM analysis, which increased the particle size and limited the useful resolution of the SEM. In addition, SEM measurements were performed by collecting the soot on porous filters (Nucleopore 0.2 mm pores) that might have caused biasing in the size distributions of the particles captured since smaller particles would have tended to follow the flow better through the filter.

The EAA analysis gave results that verified the range and average sizes of the soot aggregates. The EAA measured the average aggregate size as being around 30 nm, which corresponds to the range of mean aggregate diameters from the TEM analysis. This rough agreement is considered valuable in view of the divergent methods of sampling and size analysis being compared. From these comparative measurements, it was concluded that no systematic bias was identifiable for the thermophoretic sampling procedure and the image analysis technique.

SUMMARY

The thermophoretic sampling technique employing transmission electron microscopy has

been used to reveal the morphology of soot along the axis of a liquid-fueled, complex-flow reactor. Particle morphology typical of those from other combustion devices was observed. The results were repeatable, and comparison measurements suggest that the sampling and size analysis techniques are free of any systematic bias. The conclusions of this study are as follows.

1. The dominant mechanisms of soot formation with respect to axial distance in the model combustor are, for the condition considered:
   x/R = 0–5: particle nucleation without significant surface growth
   x/R = 5–10: surface growth occurring with agglomeration
   x/R = 10–15: oxidation with agglomeration.
2. The average primary particle size for this condition is observed to grow from approximately 10 nm at the first appearance of unagglomerated soot (x/R = 3) to 13.2 nm near the plane of x/R = 10. The range of these sizes is near the low end of the primary sizes observed in laminar diffusion flames, and signifies surface growth occurring from the middle to upper regions of the combustor. The extent of primary particle growth is low due to the comparatively short residence times of this combustor and possibly to competing oxidative reactions. Oxidation finally prevails from x/R = 10–15, as indicated by the gradual reduction of primary particle sizes along these heights.
3. Agglomeration of particles is revealed by increasing aggregate mean size and mean n (number of primaries per aggregate) from x/R = 3–15. The soot aggregate size distribution as defined by n is found to compare well with an equivalent lognormal distribution during the surface growth stage, but less so at the upper portions of the flame where oxidation and agglomeration dominate.
4. Fractal dimensions for the soot population at all five axial locations was determined to be approximately 1.8, suggesting the dominance of cluster–cluster agglomeration in the soot growth processes in the complex-flow combustor.

The authors gratefully acknowledge the University Energy Research Group (UERG) of the University of California for its support. We also appreciate the interest of Dr. Pat Saatzer and the support of the Northrop Corporation. Brian Bissell contributed to the design and fabrication of the facility. Dr. Grace Goo and Susan Fisher aided in the electron microscopy work. Prof. Jim Eartlman provided the use of the image analysis system.

REFERENCES

1. Glassman, I., *Twenty-Second Symposium (International) on Combustion*, The Combustion Institute, Pittsburgh, 1988, pp. 295–311.
2. Haynes, B. S., and Wagner, H. G., *Prog. Energy Combust. Sci.* 7:229–273 (1981).
3. Wood, C. P., and Samuelsen, G. S., *ASME J. Eng. for Gas Turbines and Power* 107:38–47 (1985).
4. Wood, C. P., Smith, R. A., and Samuelsen, G. S., *Twenueth Symposium (International) on Combustion*, The Combustion Institute, Pittsburgh, 1984, pp. 1083–1094.
5. Dobbins, R. A., and Megaridis, C. M., *Langmuir* 3:254–262 (1987).
6. Megaridis, C. M., Ph.D. dissertation, Brown University, 1987. Also available as Report NBS-GCR-87-532.
7. Megaridis, C. M., and Dobbins, R. A., *Twenty-Second Symposium (International) on Combustion*, The Combustion Institute, Pittsburgh, 1988, pp. 353–362.
8. Megaridis, C. M., and Dobbins, R. A., *Combust. Sci. Technol.* 66:1–16 (1989).
9. Megaridis, C. M., and Dobbins, R. A., *Combust. Sci. Technol.* 71:95–109 (1990).
10. Dobbins, R. A., and Subramaniasivam, H., in *Mechanisms and Models of Soot Formation, Lecture Notes in Physics*, Springer-Verlag, New York, 1992.
11. Koylu, U. O., and Faeth, G. M., *Combust. Flame* 89:140–156 (1992).
12. Friedlander, S. K., *Smoke Dust and Haze: Fundamentals of Aerosol Behavior*, Wiley, New York, 1977, pp. 42–44.
13. Eisner, A. D., and Rosner, D. E., *Combust. Flame* 61:153–166 (1985).
14. Rosner, D. E., Mackowski, D. W., and Garcia-Ybarra, P., *Combust. Sci. Technol.* 80:87–101 (1991).
15. Prado, G. P., Lee, M. L., Hites, R. A., Hoult, D. P., and Howard, J. B., *Sixteenth Symposium (International) on Combustion*, The Combustion Institute, Pittsburgh, 1976, pp. 649–661.

16. Himes, R. M., Hack, R. L., and Samuelsen, G. S., *ASME J. Eng. for Gas Turbines and Power* 106:103–108 (1984).
17. Samson, R. J., Mulholland, G. W., and Gentry, J. W., *Langmuir* 3:272–281 (1987).
18. Brum, R. D., and Samuelsen, G. S., *Exp. Fluids* 5:95–102 (1987).
19. Botet, R., and Jullien, R., *Aggregation and Fractal Aggregates*, World Scientific Publishing, Singapore, 1987.
20. Wersborg, B. L., Howard, J. B., and Williams, G. C., *Fourteenth Symposium (International) on Combustion*, The Combustion Institute, Pittsburgh, 1973, pp. 929–940.
21. Wey, C., Powell, E. A., and Jagoda, I. J., *Twentieth Symposium (International) on Combustion*, The Combustion Institute, Pittsburgh, 1984, pp. 1083–1094.
22. Vuk, C. T., Jones, M. A., and Johnson, J. H., *Trans. SAE* 85:556–597, Paper 760131, 1976.
23. Samuelsen, G. S., and Wood, C. P., in *NATO AGARD Conf. Proc. No. 422*, 1987, pp. 16.1–16.6.
24. Harris, S. J., and Weiner, A. M., *Combust. Sci. Technol.* 31:155–167 (1983).
25. Harris, S. J., *Combust. Sci. Technol.* 72:67–77 (1990).
26. Prado, G., Jagoda, J., Neoh, K., and Lahaye, J., *Eighteenth Symposium (International) on Combustion*, The Combustion Institute, Pittsburgh, 1981, pp. 1127–1136.
27. Chippet, S., and Gray, W. A., *Combust. Flame* 31:149–159 (1978).
28. Bockhorn, H., Fetting, F., Meyer, U., Reck, R., and Wannemacher, G., *Eighteenth Symposium (International) on Combustion*, The Combustion Institute, Pittsburgh, 1981, pp. 1137–1147.
29. Taylor, J. R., *An Introduction to Error Analysis*, University Science Books, Oxford University Press, Oxford, 1982.
30. Hines, W. W., and Montgomery, D. C., *Probability and Statistics in Engineering and Management Science*, 2nd ed., Wiley, New York, 1980, pp. 280–282, 596.
31. Sorensen, C. M., Cai, C., and Lu, N., *Langmuir* 8:2064–2069 (1992).

Received 7 November 1992; accepted 19 February 1997